ADVANCED MATERIALS
www.advmat.de

Temperature Dependence of the Piezotronic and Piezophototronic Effects in *a*-axis GaN Nanobelts

*Xingfu Wang, Ruomeng Yu, Wenbo Peng, Wenzhuo Wu, Shuti Li, and Zhong Lin Wang**

Wurtzite-structured materials with noncentrosymmetric crystal structures present piezoelectric polarizations under mechanical deformation due to the relative displacements between the centers of positive and negative ions.[1,2] In piezoelectric semiconductor materials, such as ZnO, CdS, and GaN, the mechanical strain-induced piezoelectric polarization charges (piezocharges) are created and distributed along the polar direction.[3–5] By coupling the piezoelectric and semiconducting properties of these materials, piezoelectric polarizations are utilized to modulate the charge carriers transport processes in piezoelectric semiconductors under externally applied strains, which are referred to as the piezotronic effect.[6–8] Furthermore, the piezophototronic effect[9–11] is introduced as a three-way coupling among piezoelectric polarization, semiconductor property, and optical excitation by applying piezocharges presented at the vicinity of the local interface to control/tune the optoelectronic processes of charge carriers, such as generation, separation, recombination, and transport within piezoelectric semiconductors. These two emerging effects are fundamentally new in physics and have drawn increasing research interests recently and led to both novel fundamental phenomenon and unprecedented device characteristics as well as applications in various fields, including strain sensor,[12,13] logic computations,[14–16] photodetectors,[17,18] solar cells,[19] and light emitting diodes.[20,21]

Considering the preferential polar growth direction (typically *c*-axis) of 1D semiconductor nanostructures, in most reported piezotronic/piezophototronic devices, the piezocharges are presented at the vicinity of the local interface at both ends of the nanostructures along the polar axis and utilized to modulate the barrier height/energy band profile at the junction region, such as metal–semiconductor (M–S) junction[22–24] and homo-/hetero-junction.[25–27] However, due to the relatively small effective junction area and weak optical absorptions, the performance and application of piezotronic/piezophototronic devices may thus be restricted. By synthesizing the nanotructures along the nonpolar *a*-axis orientation, the charge carriers transport processes of piezoelectric semiconductors are modulated by the piezotronic/piezophototronic effects within the entire body of the nanostructure, since the piezocharges created upon straining are distributed along the whole polar surfaces that are perpendicular to the *c*-axis. Therefore, it is of great significance to systematically investigate the physical working mechanism of both the piezotronic and piezophototronic effects in nanostructures synthesized along the nonpolar *a*-axis not only for understanding the fundamentals, but also for guiding the design and developments of high-performances piezotronic/piezophototronic devices based on *a*-axis nanostructured piezoelectric semiconductors in the future.

Here, the temperature dependence of both the piezotronic and piezophototronic effects is investigated in GaN nanobelts (NBs) synthesized along the nonpolar *a*-axis orientation. As cooling the system from 300 to 77 K, the piezotronic effect in *a*-axis GaN is enhanced by over 440% owing to the increased effective piezoelectric polarizations resulted from the reduced screening effect caused by the decreased charge carriers mobility and density. The corresponding piezopotential distributions, the energy band diagrams and the depletion region induced by the piezocharges are calculated via finite element analysis (FEA) at various temperatures. Besides, two independent processes are discovered to form a competing mechanism through the investigation of the temperature dependence of the piezophototronic effect in *a*-axis GaN. The corresponding energy band diagrams at both low and room temperatures are carefully analyzed to explain the working mechanism of the piezophototronic effect at different temperatures. This study presents in-depth understandings about the temperature dependence of the piezotronic and piezophototronic effects in *a*-axis GaN and provides guidance to their potential applications in high-performances electromechanical/optoelectronic devices.

GaN NBs used in this work are synthesized on patterned silicon substrates by a metal–organic chemical vapor deposition system as described elsewhere.[28] A typical scanning electron microscope (SEM, Hitachi SU8010) image of the as-synthesized GaN NB is shown in **Figure 1**a1, with the length ranging from tens of micrometers to several hundred micrometers. The corresponding atomic structure model (top view) of the GaN NB is shown in Figure 1a2, indicating the GaN NB is synthesized along the nonpolar $\langle 2\bar{1}\bar{1}0\rangle$ (i.e., *a*-axis) direction as detailed characterized in our previous work.[28,29] The noncentrosymmetric wurtzite single crystal structure of GaN NBs is confirmed by the selected area electron diffraction (SAED, Tecnai G2) patterns indexed along the *a*-axis (Figure 1a3) and

X. Wang, R. Yu, W. Peng, Dr. W. Wu, Prof. Z. L. Wang
School of Materials Science and Engineering
Georgia Institute of Technology
Atlanta, GA, 30332-0245, USA
E-mail: zhong.wang@mse.gatech.edu
X. Wang, Prof. S. Li
Guangdong Engineering Research Center of
Optoelectronic Functional Materials and Devices
South China Normal University
Guangzhou 510631, China
Prof. Z. L. Wang
Beijing Institute of Nanoenergy and Nanosystems
Chinese Academy of Sciences
Beijing 100083, China

DOI: 10.1002/adma.201504534

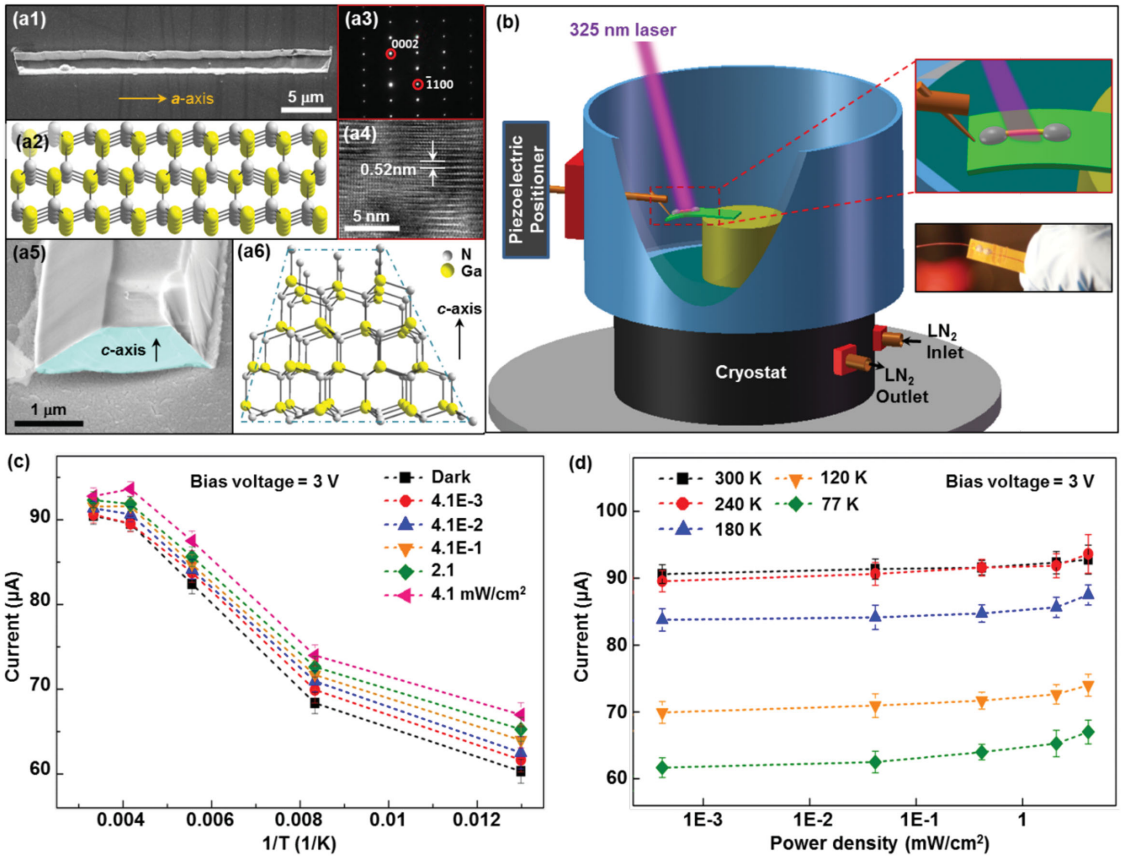

Figure 1. Structure characterizations and current response of GaN NBs devices. a1) SEM image and a2) the corresponding atomic model of the GaN NB synthesized along *a*-axis. a3) SAED pattern, a4) HRTEM image, a5) SEM image, and a6) the corresponding atomic model of the cross section of the *a*-axis GaN NB. b) Schematic illustration of the experimental set-up and the digital image of a real device. Under strain-free conditions and a bias voltage of 3 V, c) the current response of GaN NB devices to various temperatures and d) illumination intensities.

the corresponding high-resolution transmission electron microscope (HRTEM, FEI F30) image (Figure 1a4), with the polar *c*-axis pointing to the top surface of the GaN NB. The enlarged SEM image of the trapezoid-shaped end surface and the corresponding atomic structure model are shown in Figure 1a5,a6, respectively.

The piezotronic and piezophototronic effects on the electric transport properties of *a*-axis GaN NBs-based devices are measured in a micro-manipulation cryogenic probe system (Janis, model ST-500-2) as schematically illustrated in Figure 1b. By circulating liquid nitrogen through the cryostat of the measurement system, the temperature of the chamber is controlled between 77 and 300 K. Reliable thermal equilibrium between the GaN NB and the cryostat is achieved by adopting aluminum foils (76 μm in thickness) covered with a layer of Kapton tape (30 μm in thickness) as the substrate (1 cm × 3 cm), which features with excellent thermal conductivity, an insulating surface and satisfactory mechanical flexibility. The thermal expansion coefficients of aluminum and Kapton tape are 23.1 × 10^{-6}/°C and 20 × 10^{-6}/°C,[30] respectively. Substrate deformations due to the mismatch of thermal expansion coefficients can therefore be neglected. The device is fabricated by transferring and bonding an individual GaN NB laterally on this substrate with its *a*-axis parallel to the long edge. Silver paste is applied to fix both ends of the NB, serving as source and drain electrodes. A digital image of the as-fabricated *a*-axis GaN device is shown in the lower right of Figure 1b. One end of the device is fixed on the sample mount (Figure 1b, upper right) of the probe station system with the other end free to be bent. Mechanical strains are introduced through a micro-manipulating probe attached to one of the probing station arms moving in three dimensions. The values of the externally applied tensile strains are calculated following the method reported previously by Yang et al.[31] A beam of 325 nm UV laser is introduced to provide optical stimuli for characterizing optoelectronic performances of the GaN NB devices under a series of strains with the temperature varying from 77 to 300 K. The electric output signals are measured and collected by computer-controlled program through a GPIB controller; details are found in the Experimental Section.

Under strain-free condition and a bias voltage of 3 V, the current response of the GaN NB devices to various temperatures (illumination intensities) at different illumination intensities (temperatures) are summarized and plotted in Figure 1c,d. Higher output currents are observed under stronger illumination intensities at each temperature (Figure 1d) since more charge carriers are generated by stronger optical stimuli. Furthermore, under certain illumination intensity, the current response increases drastically with the temperature from 77 to 240 K as shown in Figure 1c due to the gradually release of freeze-out carriers on shallow donor energy states. No significant current increase, however, is observed when the temperature

Adv. Mater. **2015**,
DOI: 10.1002/adma.201504534

increases from 240 to 300 K. It is because most of the trapped charge carriers are released at about 200 K,[32,33] as heating up the system to 300 K, enhanced scattering by the lattice vibration decreases the mobility of free charge carriers[34] and thus reduce the conductivity of the GaN NB devices.

Temperature dependence of the piezotronic effect in *a*-axis GaN is systematically investigated by applying a series of mechanical strains to the device at various temperatures and dark condition. *I–V* characteristics of *a*-axis GaN devices are measured at 300 K (**Figure 2**a), 240 K (Figure S1a, Supporting information), 180 K (Figure S1b, Supporting information), 120 K (Figure 2b), and 77 K (Figure 2c) by externally applying strains ranging from 0% to 0.28%. Obviously, the output currents decrease as applying more tensile strains at each temperature condition but with distinguishable magnitudes. As the system temperature decreases, the changes of *I–V* curves become more and more significant, and the difference among output currents derived under various tensile strains become the most explicit at 77 K. These observed experimental results are caused by increased effective piezoelectric polarization charges at low temperature due to the reduced screening effect by free charge carriers, since more mobile charges are trapped in the shallow impurities centers (i.e., freeze-out effect) at lower temperature. In order to quantitatively characterize the temperature dependence of the piezotronic effect in *a*-axis GaN NB devices, a gauge factor is defined as the relative changes of output currents per unit strain: $dI/(I_0\Delta\varepsilon) = (I_\varepsilon - I_{\varepsilon=0\%})/(I_{\varepsilon=0\%}\,\varepsilon)$, where I_ε and $I_{\varepsilon=0\%}$ correspond to the output currents under strain ε and strain-free condition, respectively. The corresponding piezotronic gauge factors are calculated at different temperatures and straining conditions as plotted in Figure 2d. The results indicate that the piezotronic effect is enhanced by over 440% as the system temperature decreasing from 300 to 77 K under 0.28% tensile strains. The obtained enhancement presents similar trend as reported in previous investigations on the temperature dependence of the piezotronic effect in *c*-axis ZnO[14] nanowires, where the effective piezoelectric polarizations are also increased by cooling the system.

The physical mechanism of temperature dependence of the piezotronic effect is carefully studied by theoretical simulations via FEA as shown in Figure 3 and Figure S2a (Supporting Information). The mechanical equilibrium and the direct piezoelectric effect are given by[35]

$$\begin{cases} \sigma_{\mathbf{p}} = c_{\mathrm{pq}}\varepsilon_{\mathrm{q}} - e_{\mathrm{pk}}E_{\mathrm{k}} \\ D_{\mathrm{i}} = e_{\mathrm{iq}}\varepsilon_{\mathrm{q}} + K_{\mathrm{ik}}E_{\mathrm{k}} \end{cases} \quad (1)$$

where σ is the stress tensor, ε is the strain tensor, E is the electric field, D is the electric displacement, κ_{ik} is the dielectric constant, e_{iq} is the piezoelectric constant, and c_{pq} is the mechanical

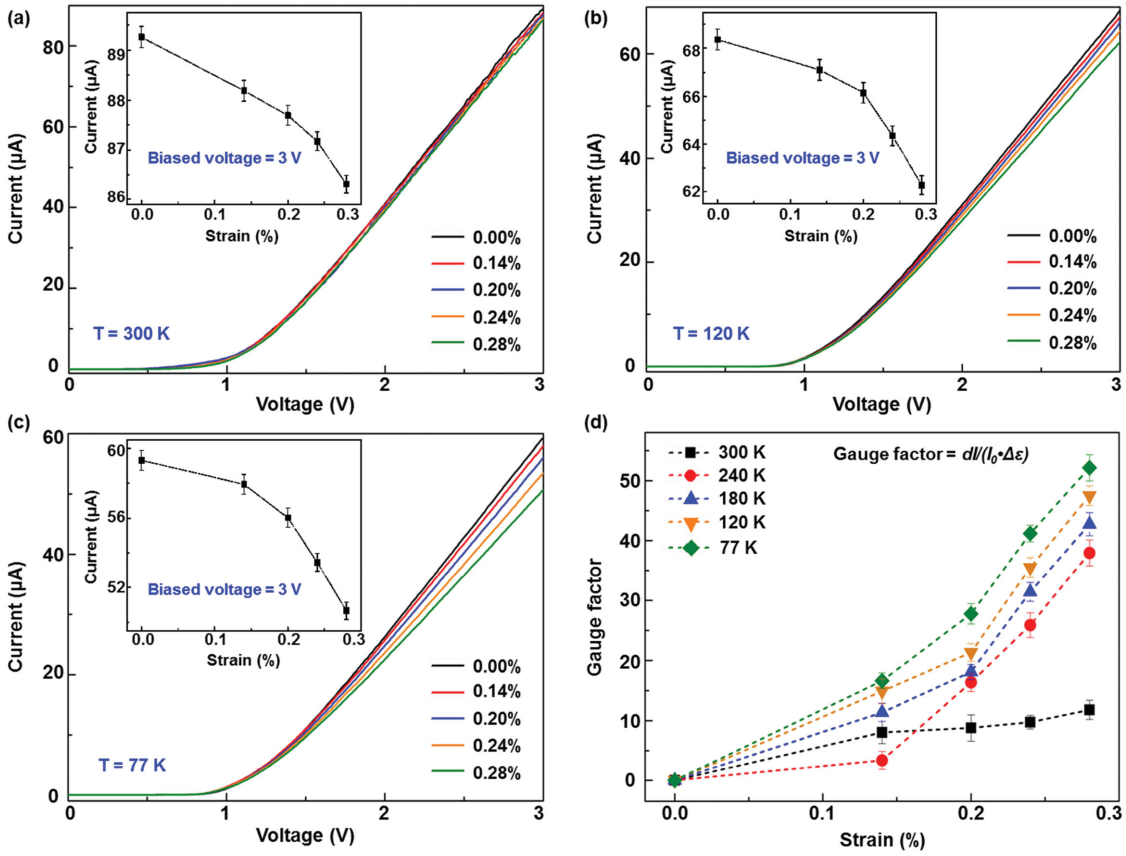

Figure 2. Temperature dependence of the piezotronic effect in *a*-axis GaN NB. Under dark conditions, the piezotronic effect on the *I–V* characteristics of the GaN devices at a) 300 K, b) 120 K, and c) 77 K. The insets are the corresponding current responses to various strains at 3 V biased voltage. d) Gauge factor $dI/(I_0\Delta\varepsilon)$ versus the applied strains at a series of temperatures.

DOI: 10.1002/adma.201504534

stiffness tensor. The Voigt–Nye notation is used. By substituting the second equation into Gauss's law, the equation for the electric field is derived as

$$\nabla D = \frac{\partial}{\partial x_i}\left(e_{iq}\varepsilon_q + K_{ik}E_k\right) = \rho = e\left(p - n + N_D^+ - N_A^-\right) \quad (2)$$

where p is the hole concentration in the valence band, n is the electron concentration in the conduction band, N_D^+ is the ionized donor concentration, and N_A^- is the ionized acceptor concentration, $p = N_A^- = 0$ is adopted for n-type GaN nanobelts used in this work. Therefore equation (2) can be rewritten as:

$$\nabla D = \frac{\partial}{\partial x_i}\left(e_{iq}\varepsilon_q + K_{ik}E_k\right) = \rho = e\left(-n + N_D^+\right) \quad (3)$$

The redistribution of electrons under thermodynamic equilibrium is given by the Fermi–Dirac statistics

$$\begin{cases} n = N_c \dfrac{2}{\sqrt{\pi}} \displaystyle\int_{E_c(x)}^{\infty} \frac{\left[\left(E - E_c(x)\right)/kT\right]^{1/2}}{1 + \exp\left[\left(E - E_F\right)/kT\right]} \frac{dE}{kT} \\ N_c = 2\left(\dfrac{2\pi m_e kT}{h^2}\right)^{3/2} \end{cases} \quad (4)$$

where the conduction band edge $E_c(x)$ is a function of space coordinates. N_c, the effective state density of conduction band, is determined by the effective mass of conduction band electrons m_e and temperature T. Considering the significant strains applied upon the GaN NBs, the band edge shift ΔE_c is expressed by the electrostatic energy part and the deformation potential part

$$\Delta E_c = E_c - E_{c0} = -e\varphi + \Delta E_c^{\text{deform}} = -e\varphi + a_c \frac{\Delta V}{V} \quad (5)$$

where E_{c0} is the conduction band edge of a strain-free GaN NB; $\Delta E_c^{\text{deform}} = a_c \Delta V/V$ is the band edge shift caused by the deformation potential,[36] which is proportional to the relative volume change $\Delta V/V$, and a_c is the deformation potential constant. Finally, the activation process of the donors is given by

$$N_D^+ = N_D \frac{1}{1 + 2\exp\left(\dfrac{E_F - E_D(x)}{kT}\right)} \quad (6)$$

where $E_D(x) = E_c(x) - \Delta E_D$ is the position-dependent donor energy level. The constant ΔE_D is the activation energy of the donors. N_D is the temperature-dependent doping level in GaN and calculated via a well-developed Matlab based program PKUMSM[37] by fitting the I–V characteristics in Figure 2 and Figure S1 (Supporting Information) at 300, 240, 180, 120, and 77 K. Details are found in the Experimental Section. By solving the nonlinear partial differential Equations (1–6) via FEA, the piezopotential distributions (**Figure 3**a), energy band diagrams

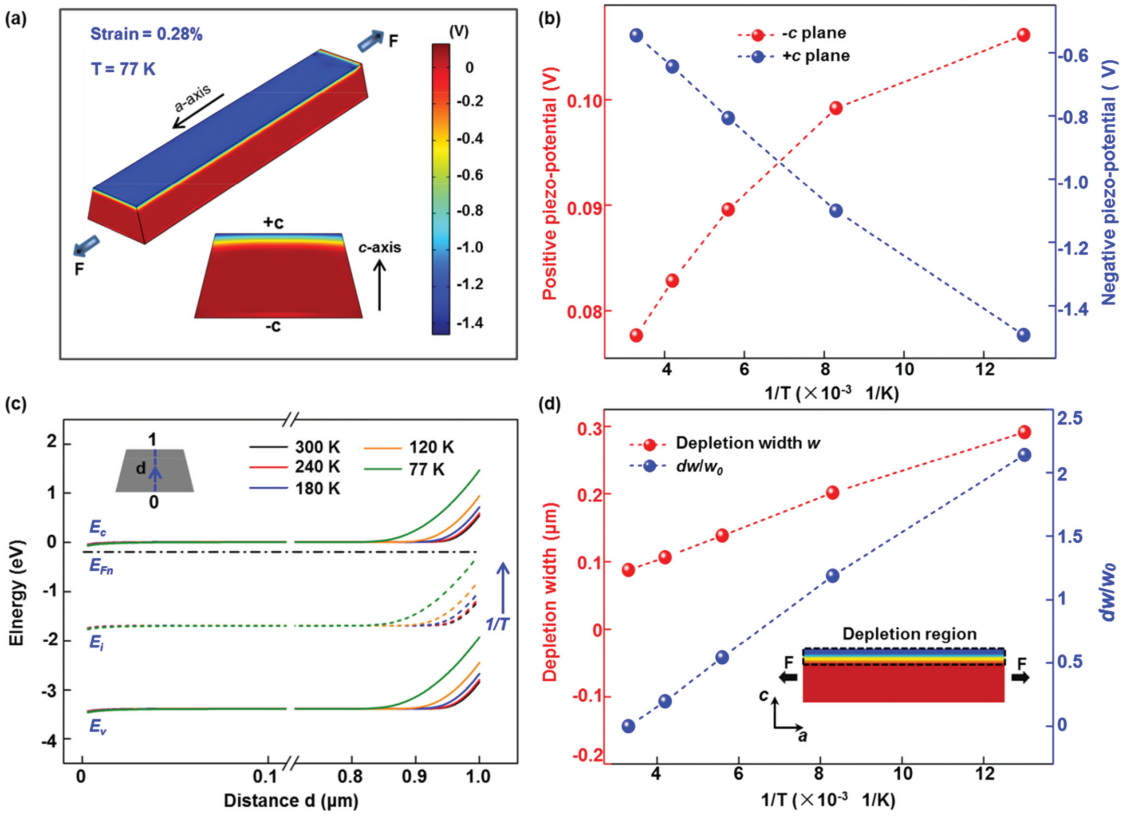

Figure 3. Theoretical simulations of the temperature dependence of the piezotronic effect. a) Finite element simulation of the piezoelectric potential distribution in the *a*-axial GaN NB under 0.28% tensile strain along *a*-axis at 77 K. b) The piezoelectric potential at +*c* plane (blue) and –*c* plane (red) as a function of the system temperature. c) Energy band diagrams of *a*-axis GaN NB at different system temperatures under 0.28% tensile strain. d) Electron depletion width (red) and its relative changes (blue) near the +*c* plane at different temperatures under 0.28% tensile strain.

Adv. Mater. **2015**,
DOI: 10.1002/adma.201504534

(Figure 3c), and local carrier concentrations (Figure S2a, Supporting Information) in *a*-axis GaN NB are derived. Detailed simulation parameters are found in the Experimental Section.

Under 0.28% tensile strains, the piezopotential distribution in *a*-axial GaN NB at 77 K is simulated and presented in Figure 3a with the overall view (upper) and cross-section view (lower), showing that positive piezopotential is induced at $-c$ plane and negative piezopotential at $+c$ plane. The corresponding piezopotential values at both $+c$ and $-c$ planes are extracted from Figure 3a and plotted in Figure 3b as a function of temperatures. Generally, the absolute values of the effective negative piezopotential are one order of magnitude larger than those of the effective positive piezopotential. This is because the free electrons with relatively high mobility in GaN NB screen most of the positive piezopolarizations, while the negative piezopolarizations are only partially screened considering the poor mobility of positive ionized donors $\left(N_D^+\right)$. Besides, as decreasing the temperature from 300 to 77 K, both the negative and positive piezopotential increases due to the reduced screening effect, since more electrons/N_D^+ are trapped at lower temperature to reduce the density of free charge carriers. Furthermore, the noncompletely screened negative piezopotential presented near $+c$ plane effectively repulse the free electrons and produce an electron depletion region to modify the conducting channel width of *a*-axis GaN NB controlled by the external strains. The corresponding energy band diagrams and local carrier concentrations under 0.28% tensile strains at various temperatures are calculated and plotted in Figure 3c and Figure S2a (Supporting Information). By locating the bending point of energy band diagrams (Figure 3c) and carrier density distributions (Figure S2a, Supporting Information), the electron depletion region width under 0.28% strain is determined[34] and plotted in Figure 3d. It is obvious that the depletion region width w (Figure 3d, red) increases as decreasing the system temperature. Moreover, the relative changes of w is defined as $dw/w_0 = (w_T - w_{T0})/w_{T0}$, where w_T and w_{T0} are the depletion region width at temperature T and T_0 = 300 K, respectively, and plotted in Figure 3d (blue) as well. These results further confirm that the piezotronic effect is significantly enhanced at low temperature.

Temperature dependence of the piezophototronic effect on the output currents of GaN NB devices is carefully studied under a series of light illuminations and straining conditions from 77 to 300 K as shown in **Figure 4**. Photocurrents ($I_{photo} = I_{light} - I_{dark}$) are calculated to evaluate the change of current response to various UV illuminations at 300 K (Figure 4a), 240 K (Figure S2b, Supporting Information), 180 K (Figure S2c, Supporting Information), 120 K (Figure 4b), and 77 K (Figure S2d, Supporting Information). These results clearly show that, at 300 and 240 K, the photocurrents I_{photo} increase monotonically as increasing the tensile strains, although there exist fluctuations

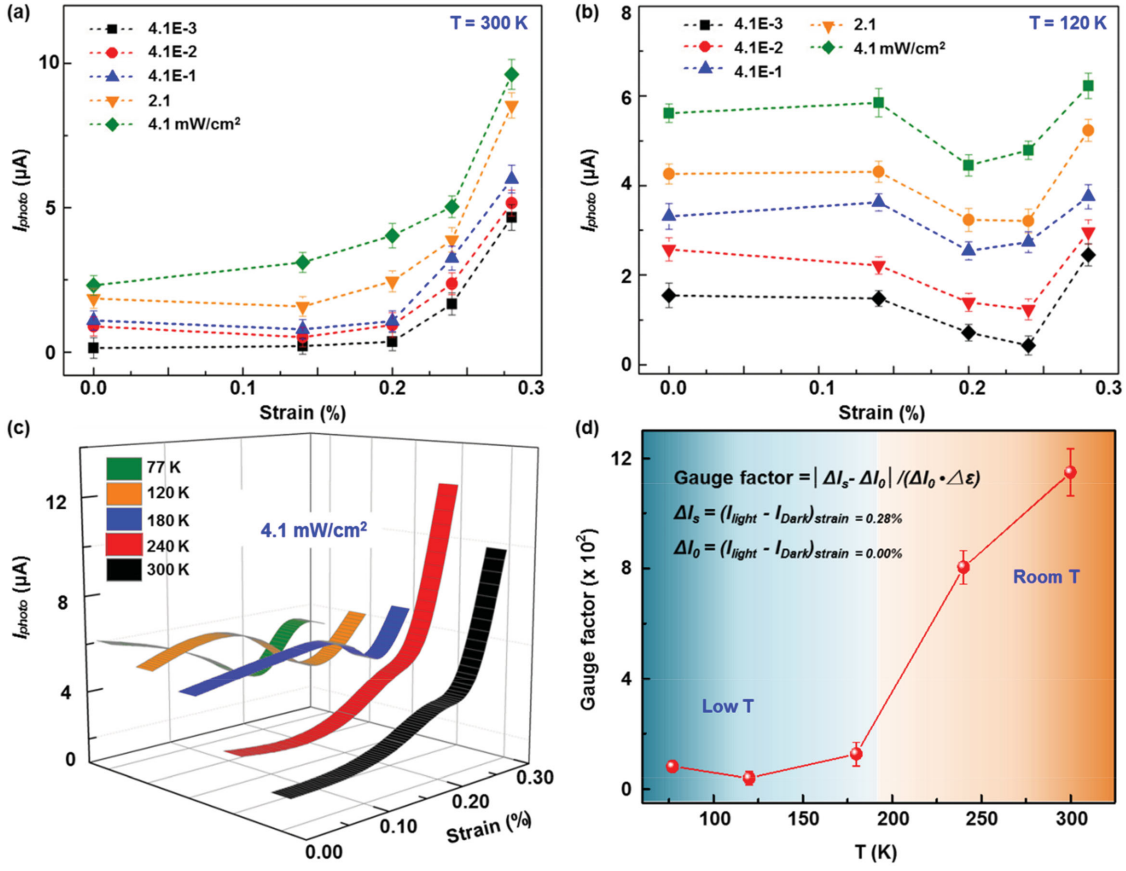

Figure 4. Temperature dependence of the piezophototronic effect in *a*-axis GaN NB. Photocurrent versus externally applied strains under a series of illumination intensity at a) 300 and b) 120 K. c) Under the illumination identity of 4.1 mW cm^{-2}, the photocurrent ($I_{photo} = I_{light} - I_{dark}$) versus tensile strains at various temperatures. d) Photocurrent gauge factor as a function of system temperature.

under weak illuminations and small straining conditions; while at low temperature of 180, 120, and 77 K, I_{photo} decrease as increasing strains at first and then increase with a local minimum observed at a certain straining condition. Under 4.1 mW cm^{-2} illumination identity, the photocurrent I_{photo} as a function of tensile strains at various temperatures are summarized and shown in Figure 4c. The temperature dependence of the piezophototronic effect is quantitatively evaluated by defining a photocurrent gauge factor as the changes of photocurrent per unit strain: $|\Delta I_1 - \Delta I_0|/(\Delta I_0\ \Delta\varepsilon)$, where ΔI_1 and ΔI_0 correspond to the photocurrent of devices under 0.28% and 0.00% strains, respectively. Figure 4d shows that the value of photocurrent gauge factor remains small below 180 K and increases significantly at 240 and 300 K, with the value at 300 K more than 14 times in magnitude larger than that at 77 K. These results suggest that in the *a*-axis GaN NB devices, the enhancement of photocurrent by the piezophototronic effect at room temperature is more significant than that at low temperature. The previously reported temperature dependence of the piezophototronic effect in *c*-axis CdS nanowire[38] exhibited an completely opposite trend, in which the piezophototronic effect was significantly enhanced as cooling down the temperature from 300 to 77 K. This novel observation presented here indicates that the physical mechanism of temperature dependence of the piezophototronic effect is different in *a*-axis nanostructures compared to that in *c*-axis nanostructures.

Energy band diagrams across the width of GaN NBs along *c*-axis are schematically presented in **Figure 5** to systematically explain the temperature dependence of the piezophototronic effect in *a*-axis GaN. At room temperature, under strain-free condition, both photo-generation and recombination of electron–holes occur normally upon 325 nm UV illumination as shown in Figure 5a1. By applying compressive strains along the *c*-axis (i.e., tensile strains along the *a*-axis), under dark condition, positive piezocharges induced at the –*c* plane are screened by local free electrons in GaN, while the negative piezocharges at +*c* plane are only partially screened and thus tilt the energy band as shown in Figure 5b1. Upon UV illuminations (Figure 5c1), the photo-generated holes are readily attracted by the negative piezocharges and the recombination of electron–hole pairs is therefore greatly suppressed. As a result, the unpaired photo-excited electrons drift along *a*-axis direction under the bias voltage and are collected at the anode to contribute to the photocurrent I_{photo}. By increasing the externally applied strains, more photo-generated holes are attracted by increased negative piezocharges, leaving more unpaired photo-generated electrons to contribute to the I_{photo}. Therefore, the I_{photo} monotonically increase with the external strains at room temperature as experimentally observed in Figure 4a,c and Figure S2b (Supporting Information).

At low temperature, under strain-free condition (Figure 5a2), some free electrons are trapped in impurities centers due to the freeze-out effect,[39] leading to reduced carrier density and output currents compared to those at room temperature as shown in Figure 1c. The activation energy of these impurities is typically 20–30 meV,[32,40] which is much smaller than the energy of the incident 325 nm UV laser. Consequently, the

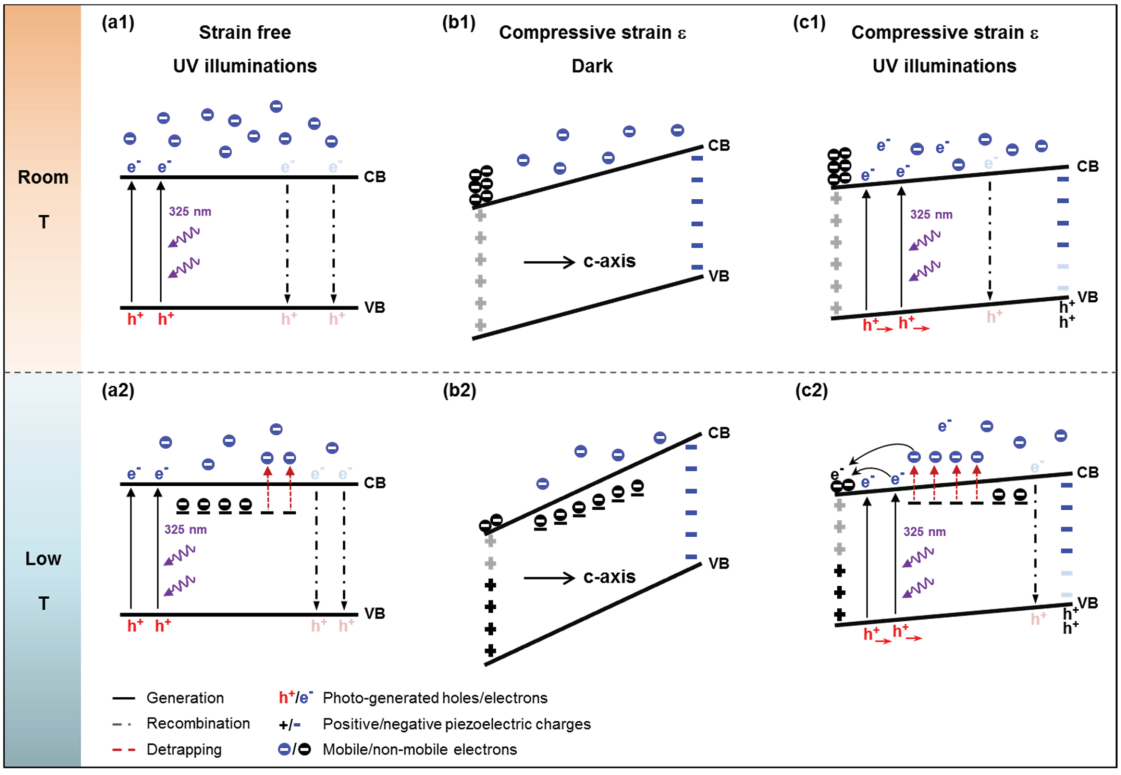

Figure 5. Working mechanisms of temperature dependence of the piezophototronic effect. At room temperature, the energy band diagram under a1) strain-free condition, compressive strains along the *c*-axis b1) in dark and c1) UV illuminations. At low temperature, the energy band diagram under a2) strain-free condition, compressive strains along the *c*-axis b2) in dark and c2) UV illuminations.

Adv. Mater. **2015**,
DOI: 10.1002/adma.201504534

trapped electrons are detrapped/activated back into conduction band by absorbing the photon energy under UV illuminations (Figure 5a2). In this scenario, the photo current I_{photo} consist of both the bandgap excitation and the detrapping/activation of the bounded electrons. In contrast, no defect related detrapping/activation process exists at room temperature since the vast majority of electrons are inherently ionized.[34] Therefore, under strain-free condition, the I_{photo} at low temperature is larger than that at room temperature as shown in Figure 4c. By applying compressive strains along the *c*-axis (i.e., tensile strains along the *a*-axis), positive and negative piezoelectric polarization charges are induced near $-c$ and $+c$ plane, respectively. At low temperature under dark condition, the positive piezocharges are only partially screened due to the decreased density and mobility of free electrons caused by the freeze-out effect, leading to a more significant tilting of energy band than that at room temperature, as shown in Figure 5b2. Upon UV illuminations (Figure 5c2), two processes form a competition mechanism: (i) Part of the photo-generated electrons and/or free electrons tend to be attracted by the noncompletely screened positive piezocharges near $-c$ plane. This process reduces the photocurrent I_{photo}. (ii) The obviously tilted energy band caused by piezoelectric polarizations makes the donor energy level closer to or into the conduction band; the detrapping/activation of bounded electrons is thus greatly enhanced under UV illuminations. More detrapped/activated electrons contribute to the I_{photo} and this process increases the photocurrent I_{photo}. In addition, as increasing the external strains, both process (i) and (ii) are enhanced. The increasing of effective positive polarization charges leads to a more significant tilting energy band. This, in turn, facilitates the trapping of photo-generated electrons and/or free electrons at the positive piezocharges side. Therefore, a local minimum of I_{photo} is observed with the increasing of strains by considering the competition mechanism between these two processes at low temperature.

Based on the experimental results and the theoretical analysis provided above, it is clear to see that under mechanical strains, the piezocharges of *a*-axis GaN NB are induced at the polar faces ($+c$ and $-c$ planes) along the *c*-axis direction. The energy band profile, charge carrier distributions and the transport property of *a*-axis GaN are modulated in the whole body of the NB as a volumetric effect. This is fundamentally distinguishable from the piezotronic/piezophototronic effects in *c*-axis nanostructures, which are interfacial effects with the piezoelectric polarizations created at the local metal-semiconductor contact formed near the end faces of the nanostructures to tune/control the carriers transport across the interface.

In conclusion, the temperature dependence of the piezotronic and piezophototronic effects is systematically investigated in GaN NBs synthesized along the nonpolar *a*-axis orientation. As cooling the system from 300 to 77 K, the piezotronic effect in *a*-axis GaN is enhanced by over 440% owing to the increased effective piezoelectric polarizations resulted from the reduced screening effect caused by the decreased charge carriers mobility and density. The corresponding piezopotential distributions, the energy band diagrams, the charge carrier concentrations, and the width of depletion region induced by the piezopolarizations are calculated via FEA at various temperatures. Moreover, the temperature dependence of the piezophototronic effect in *a*-axis GaN is carefully investigated as well and two independent processes are discovered to form a competing mechanism at low temperature, leading to a local minimum of output currents at certain straining condition. The corresponding energy band diagrams at both low and room temperatures are carefully analyzed to explain the working mechanism of the piezophototronic effect at different temperatures. This study presents in-depth understandings about the temperature dependence of the piezotronic and piezophototronic effects in *a*-axis GaN and provides guidance for their potential applications in high-performances electromechanical/optoelectronic devices.

Experimental Section

Electric Signals Measurements: A function generator (Model no. DS345, Stanford Research Systems, Inc.) and a low-noise current preamplifier (Model No. SR570, Stanford Research Systems, Inc.) were used for electrical measurements. Computer-controlled measurement software in conjunction with a GPIB controller (GPIB-USB-HS, NI 488.2) was used to collect and record the data.

Theoretical Simulation: The GaN NB was modeled as a trapezoid prism with edge length of 20 μm, the height and two base of the trapezoidal cross section was 1, 1.5, and 2 μm, respectively. The material constants of GaN, including the density ρ, the mechanical stiffness constants c_{pq}, the piezoelectric constants e_{iq}, and the dielectric constants κ_{ik} used in the FEA simulations were obtained from a previous literature.[41] Effective mass was $m_e = 0.2\ m_0$, deformation potential constants were $a_{c1} = -6.5$ eV and $a_{c2} = -11.8$ eV.[42] A boundary displacement defined by the strain in *a*-axis direction is applied at one end of the GaN NB with the other end fixed.

The temperature dependence was included by calculating the effective doping profile in GaN at different temperatures through a well-developed Matlab based program PKUMSM[30] by fitting the *I*–*V* characteristics derived at each temperature condition. The calculated doping levels were $N_D = 2 \times 10^{17}$ cm^{-3} ($T = 300$ K), 1.6×10^{17} cm^{-3} (240 K), 1.2×10^{17} cm^{-3} (180 K), 0.8×10^{17} cm^{-3} (120 K), and 0.6×10^{17} cm^{-3} (77 K). These results were plugged into Equation (6) to simulate the temperature dependence of the piezotronic effect in *a*-axis GaN NB by FEA software COMSOL Multiphysics.

Supporting Information

Supporting Information is available from the Wiley Online Library or from the author.

Acknowledgements

X.W., R.Y., and W.P. contributed equally to this work. This research was supported by the U.S. Department of Energy, Office of Basic Energy Sciences (Award DE-FG02-07ER46394) (personal, measurements).

Received: September 15, 2015
Revised: October 1, 2015
Published online:

[1] Z. L. Wang, J. H. Song, *Science* **2006**, *312*, 242.
[2] W. Z. Wu, C. F. Pan, Y. Zhang, X. N. Wen, Z. L. Wang, *Nano Today* **2013**, *8*, 619.
[3] M. Y. Choi, D. Choi, M. J. Jin, I. Kim, S. H. Kim, J. Y. Choi, S. Y. Lee, J. M. Kim, S. W. Kim, *Adv. Mater.* **2009**, *21*, 2185.

[4] L. Dong, S. M. Niu, C. F. Pan, R. M. Yu, Y. Zhang, Z. L. Wang, *Adv. Mater.* **2012**, *24*, 5470.
[5] S. N. Cha, J. S. Seo, S. M. Kim, H. J. Kim, Y. J. Park, S. W. Kim, J. M. Kim, *Adv. Mater.* **2010**, *22*, 4726.
[6] T. T. Pham, K. Y. Lee, J. H. Lee, K. H. Kim, K. S. Shin, M. K. Gupta, B. Kumar, S. W. Kim, *Energy Environ. Sci.* **2013**, *6*, 841.
[7] Z. L. Wang, *Mater. Today* **2007**, *10*, 20.
[8] Z. L. Wang, *Adv. Mater.* **2007**, *19*, 889.
[9] Q. Yang, X. Guo, W. H. Wang, Y. Zhang, S. Xu, D. H. Lien, Z. L. Wang, *ACS Nano* **2010**, *4*, 6285.
[10] Z. L. Wang, *Nano Today* **2010**, *5*, 540.
[11] S. G. Xu, W. H. Guo, S. W. Du, M. M. T. Loy, N. Wang, *Nano Lett.* **2012**, *12*, 5802.
[12] J. Zhou, Y. D. Gu, P. Fei, W. J. Mai, Y. F. Gao, R. S. Yang, G. Bao, Z. L. Wang, *Nano Lett.* **2008**, *8*, 3035.
[13] X. Xiao, L. Y. Yuan, J. W. Zhong, T. P. Ding, Y. Liu, Z. X. Cai, Y. G. Rong, H. W. Han, J. Zhou, Z. L. Wang, *Adv. Mater.* **2011**, *23*, 5440.
[14] R. M. Yu, W. Z. Wu, Y. Ding, Z. L. Wang, *ACS Nano* **2013**, *7*, 6403.
[15] R. M. Yu, W. Z. Wu, C. F. Pan, Z. N. Wang, Y. Ding, Z. L. Wang, *Adv. Mater.* **2015**, *27*, 940.
[16] W. Z. Wu, Y. G. Wei, Z. L. Wang, *Adv. Mater.* **2010**, *22*, 4711.
[17] J. X. Chen, L. W. Ding, X. H. Zhang, L. Chu, N. S. Liu, Y. H. Gao, *Opt. Express* **2014**, *22*, 3661.
[18] Q. S. Hong, Y. Cao, J. Xu, H. M. Lu, J. H. He, J. L. Sun, *ACS Appl. Mater. Interfaces* **2014**, *6*, 20887.
[19] C. F. Pan, S. M. Niu, Y. Ding, L. Dong, R. M. Yu, Y. Liu, G. Zhu, Z. L. Wang, *Nano Lett.* **2012**, *12*, 3302.
[20] Q. Yang, W. H. Wang, S. Xu, Z. L. Wang, *Nano Lett.* **2011**, *11*, 4012.
[21] Q. Yang, Y. Liu, C. F. Pan, J. Chen, X. N. Wen, Z. L. Wang, *Nano Lett.* **2013**, *13*, 607.
[22] Y. F. Hu, J. Zhou, P. H. Yeh, Z. Li, T. Y. Wei, Z. L. Wang, *Adv. Mater.* **2010**, *22*, 3327.
[23] Y. F. Hu, Y. Zhang, Y. L. Chang, R. L. Snyder, Z. L. Wang, *ACS Nano* **2010**, *4*, 4962.
[24] T. Y. Wei, C. T. Huang, B. J. Hansen, Y. F. Lin, L. J. Chen, S. Y. Lu, Z. L. Wang, *Appl. Phys. Lett.* **2010**, *96*, 013508.
[25] P. Lin, X. Q. Yan, Z. Zhang, Y. W. Shen, Y. G. Zhao, Z. M. Bai, Y. Zhang, *ACS Appl. Mater. Interfaces* **2013**, *5*, 3671.
[26] F. Zhang, S. M. Niu, W. X. Guo, G. Zhu, Y. Liu, X. L. Zhang, Z. L. Wang, *ACS Nano* **2013**, *7*, 4537.
[27] K. C. Pradel, W. Z. Wu, Y. Ding, Z. L. Wang, *Nano Lett.* **2014**, *14*, 6897.
[28] X. F. Wang, J. H. Tong, X. Chen, B. J. Zhao, Z. W. Ren, D. W. Li, X. J. Zhuo, J. Zhang, H. X. Yi, C. Liu, F. Fang, S. T. Li, *Chem. Commun.* **2014**, *50*, 682.
[29] X. F. Wang, Y. Zhang, X. M. Chen, M. He, C. Liu, Y. A. Yin, X. S. Zou, S. T. Li, *Nanoscale* **2014**, *6*, 12009.
[30] Y. F. Hu, B. D. B. Klein, Y. J. Su, S. M. Niu, Y. Liu, Z. L. Wang, *Nano Lett.* **2013**, *13*, 5026.
[31] R. S. Yang, Y. Qin, L. M. Dai, Z. L. Wang, *Nat. Nanotechnol.* **2009**, *4*, 34.
[32] R. J. Molnar, T. Lei, T. D. Moustakas, *Appl. Phys. Lett.* **1993**, *62*, 72.
[33] A. F. M. Anwar, S. L. Wu, R. T. Webster, *IEEE Trans. Electron Devices* **2001**, *48*, 567.
[34] S. M. Sze, *CC/Eng. Tech. Appl. Sci.* **1982**, 27.
[35] Y. Gao, Z. L. Wang, *Nano Lett.* **2009**, *9*, 1103.
[36] W. Shan, W. Walukiewicz, J. W. Ager, K. M. Yu, Y. Zhang, S. S. Mao, R. Kling, C. Kirchner, A. Waag, *Appl. Phys. Lett.* **2005**, *86*.
[37] Y. Liu, Z. Y. Zhang, Y. F. Hu, C. H. Jin, L. M. Peng, *J. Nanosci. Nanotechnol.* **2008**, *8*, 252.
[38] R. M. Yu, X. F. W, W. Z. Wu, C. F. Pan, Y. S. Bando, N. K. Fukata, Y. F. Hu, Y. Ding, Z. L. Wang, *Adv. Funct. Mater.* **2015**, *25*, 5277.
[39] G. A. Slack, L. J. Schowalter, D. Morelli, J. A. Freitas, *J. Cryst. Growth* **2002**, *246*, 287.
[40] W. J. Moore, J. A. Freitas, G. C. B. Braga, R. J. Molnar, S. K. Lee, K. Y. Lee, I. J. Song, *Appl. Phys. Lett.* **2001**, *79*, 2570.
[41] W. Soluch, E. Brzozowski, M. Lysakowska, J. Sadura, *IEEE Trans. Ultrason. Ferroelect. Freq. Control* **2011**, *58*, 2469.
[42] I. Vurgaftman, J. R. Meyer, L. R. Ram-Mohan, *J. Appl. Phys.* **2001**, *89*, 5815.

Adv. Mater. **2015**,
DOI: 10.1002/adma.201504534